Phys Chem Minerals (2014) 41:85–90
DOI 10.1007/s00269-013-0626-0

ORIGINAL PAPER

High-pressure elastic behavior of $Ca_4La_6(SiO_4)_6(OH)_2$ a synthetic rare-earth silicate apatite: a powder X-ray diffraction study up to 9.33 GPa

Dawei Fan · Shuyi Wei · Maining Ma · Zhiqiang Chen · Baosheng Li · Hongsen Xie

Received: 17 May 2013 / Accepted: 11 September 2013 / Published online: 21 September 2013

Abstract The compression behavior of a synthetic $Ca_4La_6(SiO_4)_6(OH)_2$ has been investigated to about 9.33 GPa at 300 K using in situ angle-dispersive X-ray diffraction and a diamond anvil cell. No phase transition has been observed within the pressure range investigated. The values of zero-pressure volume V_0, K_0, and K_0' refined with a third-order Birch–Murnaghan equation of state are $V_0 = 579.2 \pm 0.1$ Å^3, $K_0 = 89 \pm 2$ GPa, and $K_0' = 10.9 \pm 0.8$. If K_0' is fixed at 4, K_0 is obtained as 110 ± 2 GPa. Analysis of axial compressible modulus shows that the *a*-axis ($K_{a0} = 79 \pm 2$ GPa) is more compressible than the *c*-axis ($K_{c0} = 121 \pm 7$ GPa). A comparison between the high-pressure elastic response of $Ca_4La_6(SiO_4)_6(OH)_2$ and the iso-structural calcium apatites is made. The possible reasons of the different elastic behavior between $Ca_4La_6(SiO_4)_6(OH)_2$ and calcium apatites are discussed.

D. Fan (✉) · S. Wei · H. Xie
Laboratory for High Temperature and High Pressure Study of the Earth's Interior of Institute of Geochemistry, Chinese Academy of Sciences, Guiyang 550002, China
e-mail: fandawei@mails.gyig.ac.cn; fandawei@vip.gyig.ac.cn

S. Wei · M. Ma
University of Chinese Academy of Sciences, Beijing 100049, China

M. Ma
Key Laboratory of Computational Geodynamics, Chinese Academy of Sciences, Beijing 100049, China

Z. Chen
Department of Geosciences, Stony Brook University, Stony Brook, NY 11794, USA

B. Li
Mineral Physics Institute, Stony Brook University, Stony Brook, NY 11794, USA

Keywords Synchrotron X-ray diffraction · Equation of state · High pressure · $Ca_4La_6(SiO_4)_6(OH)_2$

Introduction

Apatite is a group of phosphate minerals, usually referring to hydroxyapatite, fluorapatite, and chlorapatite, named for high concentrations of OH^-, F^-, or Cl^- ions, respectively (Liu et al. 2011a). It is well known as one of the common components of terrestrial and lunar rocks as well as of meteorites, and contains significant amounts of rare earth elements (REE) and large ion lithophile elements (LILE) (Irving 1978; Matsukage et al. 2004; Watson and Green 1981). Although apatite exists primarily as an accessory phase, it is among the most important minerals in controlling rare-earth element variation in igneous rocks (Watson and Capobainco 1981; Watson and Green 1981; Watson and Harrison 1984; Hughes et al. 1991). Apatite is more sensitive than most rock-forming silicate minerals to minor changes in REE concentrations that can occur during igneous processes, and can provide important information of magmatic histories (Cherniak 2000). As naturally occurring apatites contain large amounts of the rare earth elements, it has been well known that apatite controls a large portion of the budget of these trace elements (Prowatke and Klemme 2006). Murayama et al. (1986) showed that apatites were stable at pressures and temperature conditions correspond to upper mantle of the Earth. Therefore, apatites are an important carrier of REE, LILE, and the volatile elements to the upper mantle of the Earth (Cockbain and Smith 1967; Fleet and Pan 1997; Wendt

et al. 2002). So, the thermodynamic and elastic properties of apatites are important in understanding REE and LILE behavior in the Earth's deep mantle (Matsukage et al. 2004) and are valuable in interpreting rare-earth element zoning patterns in order to gather greater insight into the histories of igneous systems. In addition, apatites are also an industrially important material with applications in catalysis, adsorbents, environmental improvement, bone replacement and ceramic membranes, and so on (Fleet et al. 2010; Fleet and Liu 2007a, b; White and Dong 2003).

In the apatite structure, the Ca ions occupy two types of nonequivalent sites: the Ca(1) sites are at the fourfold symmetry 4(*f*) position, and the Ca(2) sites are at the sixfold symmetry 6(*h*) position (Hadrich et al. 2001). The apatite structure has a high flexibility, so several metal ions can substitute for the calcium (Ca) ions in the apatite (Pan and Fleet 2002). For example, strontium (Sr), barium (Ba), and lead (Pb) can substitute for the Ca ions. Moreover, rare earth elements, such as lanthanum (La), also can easily substitute for Ca in the apatite structure (Fleet et al. 2000). The substitution of rare earth elements into apatite results in interesting electron optical phenomena and is of considerable importance in geochemistry because apatite is usually the dominant host for these trace elements in common rocks (Fleet et al. 2000). And study of rare-earth silicates provides unique insight into the influence of size of the large cation in high-pressure crystal chemistry (Fleet and Liu 2005). Moreover, rare-earth-based apatites have recently attracted considerable attention for their high oxide ion conductivities, which make them potentially useful as electrolytes for intermediate-temperature solid oxide fuel cells (Nakayama et al. 1995, 1999; Nakayama and Sakamoto 1998).

To date, the elastic properties of apatites have been investigated in a number of studies (Brunet et al. 1999; Comodi et al. 2001; Matsukage et al. 2004; Fleet et al. 2010; Fleet and Liu 2007a; Gilmore and Katz 1982; He et al. 2012; Liu et al. 2008, 2011a, b), and the site preference of rare-earth element apatites also has been reported (Fleet et al. 2000); however, there is little work on the properties and behaviors of the rare-earth element silicate apatites, such as $Ca_4La_6(SiO_4)_6(OH)_2$, under high-pressure condition (Fleet and Liu 2005; Wang et al. 2006). Moreover, high-pressure synthesis has the potential for generating new phases and material properties for compounds of rare-earth silicates (Fleet and Liu 2005). So, in the present study, we investigated the compressional behavior of a synthetic $Ca_4La_6(SiO_4)_6(OH)_2$ in situ in a diamond anvil cell under hydrostatic conditions, using synchrotron X-ray diffraction. In addition, we compared the elastic property of this study to those of apatites of different compositions.

Experiment methods

The $Ca_4La_6(SiO_4)_6(OH)_2$ sample was synthesized using a multi-anvil pressure apparatus (YJ-3000T), at the Institute of Geochemistry, Chinese Academy of Sciences, Guiyang, China. The apparatus has been described by Xie et al. (1993) in detail. The starting materials used in the synthesizing experiments were stoichiometric amounts of high purity calcium carbonate ($CaCO_3$), lanthanum oxide (La_2O_3), and silica (SiO_2). These mixtures were pretreated at 900 °C in a platinum dish for 2 h to decarbonate and then encapsulated in platinum tubes with 10 weight percent deionized water (Fleet et al. 2000). The synthesizing conditions were 2.0 GPa, 1,000 °C, and 48 h to form a single phase. The textures of the synthetic products were characterized by using optical microscopy and scanning electron microscopy (JSM-6460LV). The crystal structure if it refers to $Ca_4La_6(SiO_4)_6(OH)_2$ was confirmed by using powder X-ray diffraction method (X'Pert Pro MPD system). The composition if it refers to $Ca_4La_6(SiO_4)_6(OH)_2$ was confirmed by using electron microprobe analysis (EPMA-1600).

In this investigation, we conducted in situ high-pressure angle-dispersive X-ray diffraction experiments at the beamline X17C, National Synchrotron Light Source, Brookhaven National Laboratory. We generated the high pressure by using a symmetrical diamond anvil cell, equipped with two diamonds anvils (culet face diameter 500 μm) and tungsten carbide supports. In these high-P experiments, T301 stainless steel plates with an initial thickness of 200 μm were used as gaskets, with their central part pre-indented to a thickness of about 50 μm and then drilled through into a hole of 200 μm diameter. The finely ground $Ca_4La_6(SiO_4)_6(OH)_2$ powder plus a couple of tiny ruby balls together with a methanol/ethanol/water mixture (16:3:1), which is a hydrostatic pressure-transmitting medium up to about 10 GPa (Angel et al. 2007), were loaded into the gasket hole. The ruby fluorescence method (Mao et al. 1978) was employed to determine the experimental pressure. The wavelength of the incident synchrotron radiation beam was 0.4066 Å, and the beam size was $\sim 25 \times 20\ \mu m^2$. An online CCD detector was used to collect the X-ray diffraction patterns (collecting time = 10 min per frame), which were later integrated to generate the conventional one-dimensional profiles using the Fit2D program (Hammersley 1998). To ensure the pressure stabilities of the experiments, the pressure was stabilized for 10 min at each pressure before diffraction data measurement, and subsequently, the pressure was raised up to 9.33 GPa. Unit-cell parameters were refined by Le Bail fitting using the GSAS package (Larson and Von Dreele 2004) and user interface EXPGUI (Toby 2001) up to 9.33 GPa (Table 2). Background was fit using the Chebyshev polynomial, and X-ray peak shapes were fitted

Table 1 Observed and calculated X-ray diffraction patterns of $Ca_4La_6(SiO_4)_6(OH)_2$ at ambient conditions

h k l	d_{obs} (Å)	d_{cal} (Å)	d_{obs}/d_{cal}—1
2 0 0	4.19658	4.19696	−0.00038
1 1 1	4.00589	4.00640	−0.00051
0 0 2	3.56075	3.56037	0.00013
1 0 2	3.27756	3.27771	−0.00015
1 2 0	3.17234	3.17260	−0.00026
1 2 1	2.89681	2.89708	−0.00016
1 1 2	2.87237	2.87028	0.00040
3 0 0	2.79810	2.79797	0.00013
3 1 0	2.32859	2.32805	0.00054
1 1 3	2.13173	2.13164	0.00009
4 0 0	2.09893	2.09848	0.00045
2 2 2	2.00366	2.00320	0.00047
3 1 2	1.94874	1.94848	0.00026
1 2 3	1.90076	1.90055	0.00021
2 3 1	1.85873	1.85892	−0.00019
4 1 0	1.83177	1.83170	0.00007
4 0 2	1.80788	1.80783	0.00005
0 0 4	1.78063	1.78019	0.00044

Calculated *d*-spacings are based on the hexagonal unit-cell dimensions of $a = 9.6925$ Å and $c = 7.1207$ Å

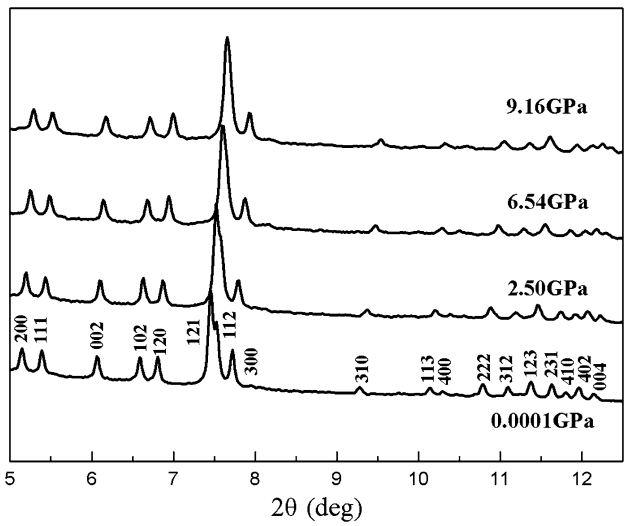

Fig. 1 Representative X-ray diffraction patterns of $Ca_4La_6(SiO_4)_6(OH)_2$ up to 9.33 GPa

using the pseudo-Voigt profile function proposed by Thomson et al. (1987).

Result and discussion

The powder X-ray diffraction data of $Ca_4La_6(SiO_4)_6(OH)_2$ at ambient conditions revealed that this phase has a hexagonal structure ($P6_3/m$), with unit-cell dimensions of $a = 9.6925(6)$ Å and $c = 7.121(1)$ Å. These values are consistent with that value reported by Cockbain and Smith (1967) (i.e., $a = 9.63$ Å, $c = 7.12$ Å). The observed and calculated X-ray diffraction patterns of $Ca_4La_6(SiO_4)_6(OH)_2$ at ambient conditions are listed in Table 1. The volume of $Ca_4La_6(SiO_4)_6(OH)_2$ at ambient conditions is 579.3(1) Å^3.

The high-pressure X-ray diffraction data were collected to 9.33 GPa at ambient temperature. Typical X-ray diffraction spectra at selected pressure are shown in Fig. 1. The diffraction patterns at each pressure of the study are similar to one another up to 9.33 GPa, with Bragg peaks shifted to higher 2θ. No phase transition occurs within the pressure range investigated. The effect of pressure on the unit-cell parameters and volume of $Ca_4La_6(SiO_4)_6(OH)_2$ are shown in Table 2. The pressure–volume data have been fitted to the third-order Birch–Murnaghan equation of state

Table 2 Cell parameters versus pressure for $Ca_4La_6(SiO_4)_6(OH)_2$

P(GPa)	*a* (Å)	*c* (Å)	*a*/*c*	*V* (Å^3)
0.0001	9.6925 (6)	7.121 (1)	1.361 (1)	579.3 (1)
0.82	9.660 (1)	7.104 (1)	1.360 (1)	574.1 (1)
1.51	9.637 (1)	7.095 (1)	1.358 (1)	570.5 (1)
2.50	9.601 (1)	7.077 (1)	1.357 (1)	565.0 (1)
4.08	9.555 (2)	7.055 (2)	1.354 (2)	557.9 (2)
5.67	9.515 (2)	7.038 (2)	1.352 (2)	551.8 (2)
6.26	9.499 (1)	7.029 (1)	1.351 (1)	549.2 (1)
8.20	9.454 (2)	7.007 (3)	1.349 (2)	542.4 (3)
9.33	9.430 (2)	6.997 (2)	1.348 (2)	538.9 (3)

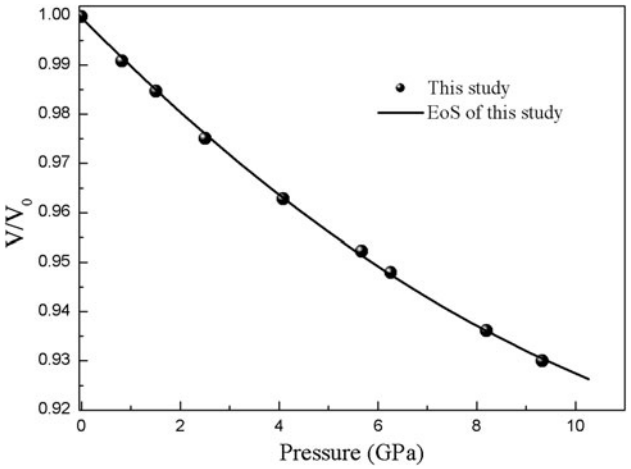

Fig. 2 Pressure–volume data for $Ca_4La_6(SiO_4)_6(OH)_2$ at 300 K. *Solid curve* third-order Birch–Murnaghan equation of state fit with K_0 and K_0' are 891 GPa and 10.9, respectively. The errors in volume are smaller than the symbols (see Table 2)

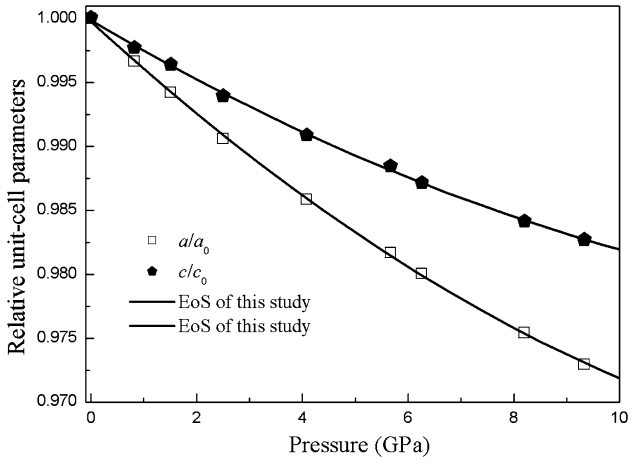

Fig. 3 Pressure dependence of the unit-cell parameters *a*, *b,* and *c* of $Ca_4La_6(SiO_4)_6(OH)_2$ at 300 K. Note that the data points of their *error bars* are smaller than the symbols

(III-BM-EoS) (Birch 1947) to determine the elastic parameters:

$$P = (3/2)\,K_0[(V_0/V)^{7/3} - (V_0/V)^{5/3}] \times \{1 + (3/4)(K_0' - 4)[(V_0/V)^{2/3} - 1]\}, \quad (1)$$

where V_0, V, K_0, and K_0' are the zero-pressure volume, high-pressure volume, isothermal bulk modulus, and its pressure derivative, respectively. The results from a least-square fitting using an EosFit program (Angel 2001) are $V_0 = 579.2(1)$ Å^3, $K_0 = 89(2)$ GPa, and $K_0' = 10.9(8)$, respectively. When K_0' is set as 4, the isothermal bulk modulus is determined as 110(2) GPa. The unit-cell volume data as a function of pressure and the compression curve calculated from these fitted parameters are plotted in Fig. 2.

The unit-cell parameters as functions of pressure are summarized in Table 2 and plotted in Fig. 3. By fitting a "linearized" third-order Birch–Murnaghan EoS, and following the procedure implemented in the EosFit 5.2 program (Angel 2001), we can obtain the axial-EoS parameters ($K_{a0} = 79 \pm 2$ GPa, $K_{a0}' = 9.3 \pm 0.7$, and $K_{c0} = 121 \pm 7$ GPa, $K_{c0}' = 16 \pm 3$ for the *a*- and *c*-axis, respectively). Then, the axial compressibilities (with $\beta_d = 1/3K_0$, where K_0 is the bulk modulus at zero pressure and room temperature, β is the compressibility, and *d* is the unit-cell parameter) from the $Ca_4La_6(SiO_4)_6(OH)_2$ P–V experimental data were found to be $\beta_a = 4.22 \times 10^{-3}$ GPa^{-1} and $\beta_c = 2.75 \times 10^{-3}$ GPa^{-1} for the *a*- and *c*-axis, respectively. The ratio between the lattice compressibility parameters, $\beta_a{:}\beta_c = 1.53{:}1$, shows that the $Ca_4La_6(SiO_4)_6(OH)_2$ sample has a compressional anisotropy. This shows excellent agreement with the conclusions of Brunet et al. (1999), Comodi et al. (2001), Matsukage et al. (2004), and Fleet et al. (2010) who considered that the *a*-axis is more compressible than the *c*-axis for hydroxyapatite, fluorapatite, and chlorapatite.

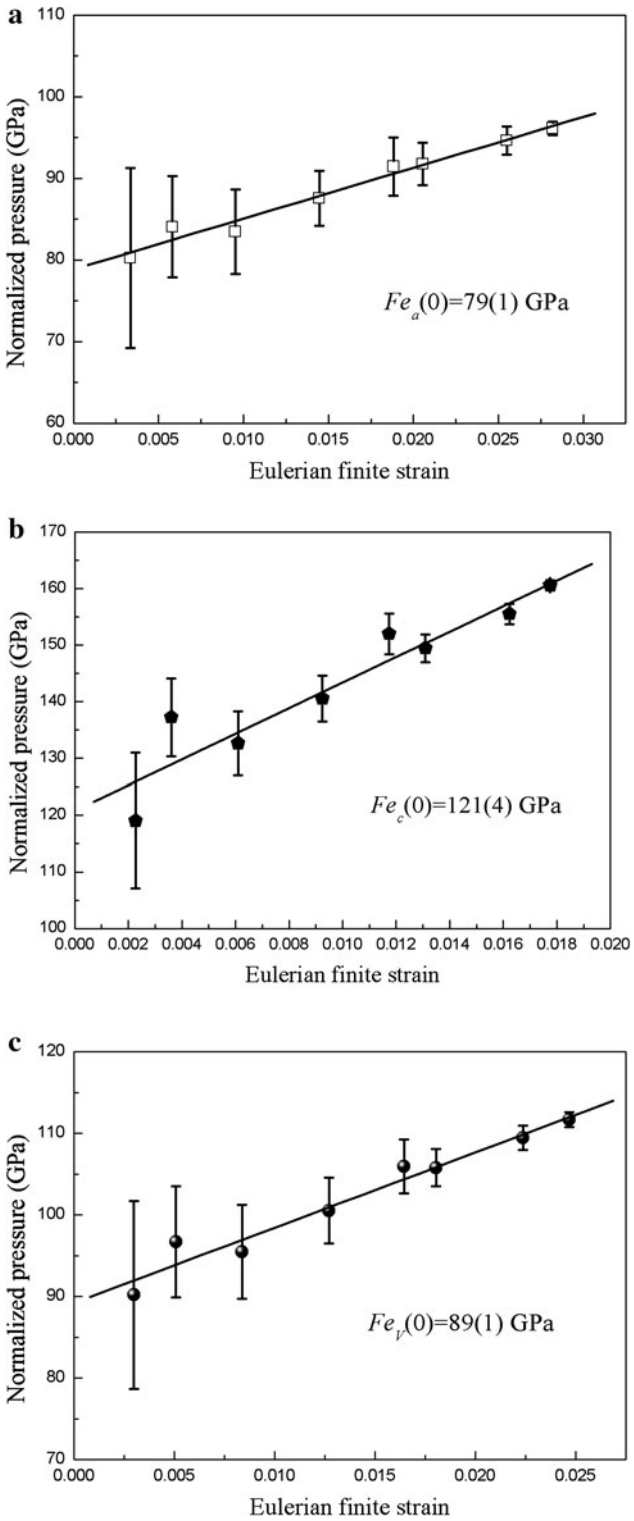

Fig. 4 Axial and volume Eulerian strain-normalized pressure (F_E–f_E) plot. The *solid lines* represent the weighted linear fit through the data

Table 3 Bulk moduli of $Ca_4La_6(SiO_4)_6(OH)_2$ and apatites

Samples	K_0 (GPa)	K_0'	References
$Ca_5(PO_4)_3OH$	97.5 (1.8)	4 (fixed)	Brunet et al. (1999)
$Ca_5(PO_4)_3F_{0.975}(OH)_{0.025}$	97.9 (1.9)	4 (fixed)	Brunet et al. (1999)
$Ca_5(PO_4)_3Cl_{0.7}(OH)_{0.3}$	93.1 (4.2)	4 (fixed)	Brunet et al. (1999)
$Ca_5(PO_4)_3F$	97.8 (1.0)	4 (fixed)	Comodi et al. (2001)
$Ca_5(PO_4)_3F$	93 (4)	5.8 (1.8)	Comodi et al. (2001)
$Ca_5(PO_4)_3F_{0.94}Cl_{0.06}$	91.5 (3.8)	4.0 (1.1)	Matsukage et al. (2004)
$Ca_4La_6(SiO_4)_6(OH)_2$	110 (2)	4 (fixed)	This study
$Ca_4La_6(SiO_4)_6(OH)_2$	89 (2)	10.9 (8)	This study

Axial and volume Eulerian finite strain ($f_E = 0.5[(V_0/V)^{2/3}-1]$) versus "normalized pressure" ($F_E = P/[3f_E(2f_E + 1)^{5/2}]$) plots ($f_E$–$F_E$ plot; Angel 2001) are shown in Fig. 4. The weighted linear regression through the data points yields the following intercept values: $Fe_a(0) = 79(1)$ GPa for the a-axis; $Fe_c(0) = 121(4)$ GPa for the c-axis; $Fe_V(0) = 89(1)$ GPa for the unit-cell volume. The slope of the regression lines is a relatively large positive slope and justifies the use of the III-BM-EoS for the axial and volume bulk moduli calculation. In addition, the normalized stress values obtained at $f_E = 0$ [i.e., $Fe_a(0)$, $Fe_c(0)$ and $Fe_V(0)$] show a very good agreement with the axial and volume bulk moduli obtained by the EoS-fit [i.e., K_0, K_{a0}, K_{c0}].

Table 3 shows a comparison of this study and the previous studies for calcium apatites at room temperature. The parameters K_0 and K_0' are usually strongly correlated in an EoS-fit (Lee et al. 2004), so we refitted the data in this study by fixing K_0' to 4.0 for purpose of comparison (Table 3). The K_0 value of 110 GPa obtained in this study for $Ca_4La_6(SiO_4)_6(OH)_2$ is substantially larger (by about 12 %) than the values of calcium apatites when K_0' is 4. The effect of substitution by F^-, Cl^-, and OH^- of calcium apatites has been studied by Brunet et al. (1999) and found to be very small (Table 3). Liu et al. (2008) considered that the effect of substitution at the BO_4 site of apatite is likely to be small since the BO_4 site cation–anion polyhedra are rigid tetrahedra. Wei et al. (2013) confirmed the inference of Liu et al. (2008) by comparing the bulk modulus of mimetite [46(7) GPa] and pyromorphite [44(5) GPa] with vanadinite [41(5) GPa, Gatta et al. 2009] and found they are similar to each other within their errors. Furthermore, the study of Serret et al. (2000) showed that La^{3+} occupied the position of Ca^{2+} ions in apatite and induced the distortion of crystal lattice or decrease in crystallite sizes. In addition, Serret et al. (2000) and Ardanova et al. (2010) found that the substitution of trivalent lanthanum for calcium in phosphate hydroxyapatite caused some interatomic distances decrease (Ca–OH from 2.380 to 2.143 Å, Ca–Ca from 4.052 to 3.711 Å, and P–O from 1.563 to 1.541 Å; Serret et al. (2000)). And they also concluded that these decreases in interatomic spacing resulted from increasing electrostatic interaction caused by substitution of highly charged ions (La^{3+}) for less-charged ions (Ca^{2+}) [Serret et al. (2000); Ardanova et al. (2010)]. Therefore, the differences in the elastic behavior of $Ca_4La_6(SiO_4)_6(OH)_2$ and calcium apatites can be mainly attributed to the substitution by large cations (La) at the Ca(2) sites of apatites (Liu et al. 2008; Zhai et al. 2011).

Conclusion

The P–V measurements on a synthetic $Ca_4La_6(SiO_4)_6(OH)_2$ at pressures up to 9.33 GPa were taken using angle-dispersive X-ray diffraction technique. The P–V equation of state for the $Ca_4La_6(SiO_4)_6(OH)_2$, fitted using the third-order Birch–Murnaghan equation of state, gives $V_0 = 579.2 \pm 0.1$ Å^3, $K_0 = 89 \pm 2$ GPa, and $K_0' = 10.9 \pm 0.8$. The axial compressibilities of the $Ca_4La_6(SiO_4)_6(OH)_2$ were determined to be 4.22×10^{-3} and 2.75×10^{-3} GPa^{-1} for the a- and c-axis, respectively. The value of the bulk modulus is larger than those of calcium apatites reported previously, which can be attributed to the substitution by large cations (La) at the Ca(2) sites of apatites.

Acknowledgments This work is supported by the National Natural Science Foundation of China (Grant Nos. 41004035, 41374107, and 41274105) and Western doctor special fund of the West Light Foundation of The Chinese Academy of Sciences (2011, to Fan Dawei), the West Light Foundation of The Chinese Academy of Sciences (to Yonggang Liu). Use of the National Synchrotron Light Source, Brookhaven National Laboratory, was supported by the US Department of Energy, Office of Science, Office of Basic Energy Sciences, under Contract No. DE-AC02-98CH10886.

References

Angel RJ (2001) Equation of state. Rev Miner Geochem 41:35–60

Angel RJ, Bujak M, Zhao J, Gatta GD, Jacobsen SD (2007) Effective hydrostatic limits of pressure media for high-pressure crystallographic studies. J Appl Crystallogr 40:26–32

Ardanova LI, Get'man EI, Loboda SN, Prisedsky VV, Tkachenko TV, Marchenko VI, Antonovich VP, Chivireva NA, Chebishev KA, Lyashenko AS (2010) Isomorphous substitutions of rare earth elements for calcium in synthetic hydroxyapatites. Inorg Chem 49:10687–10693

Birch F (1947) Finite elastic strain of cubic crystals. Phys Rev 71:809–924

Brunet F, Allan DR, Redfern SAT, Angel RJ, Miletich R, Reichmann HJ, Sergent J, Hanfland M (1999) Compressibility and thermal

expansivity of synthetic apatites, $Ca_5(PO_4)_3X$ with X = OH, F and Cl. Eur J Miner 11:1023–1035
Cherniak DJ (2000) Rare earth element diffusion in apatite. Geochim Cosmochim Acta 64:3871–3885
Cockbain AG, Smith GV (1967) Alkaline-rare-earth silicate and germanate apatites. Miner Mag 36:411–421
Comodi P, Liu Y, Zanazzi PF, Montagnoli M (2001) Structural and vibrational behaviour of fluorapatite with pressure. Part I: in situ single-crystal X-ray diffraction investigation. Phys Chem Miner 28:219–224
Fleet ME, Liu XY (2005) High-pressure rare earth silicates: lanthanum silicate with barium phosphate structure, holmium silicate apatite, and lutetium disilicate type X. J Solid State Chem 178:3275–3283
Fleet ME, Liu XY (2007a) Hydrogen-carbonate ion in synthetic high-pressure apatite. Am Miner 92:1764–1767
Fleet ME, Liu XY (2007b) Coupled substitution of type A and B carbonate in sodium-bearing apatite. Biomaterials 28:916–926
Fleet ME, Pan YM (1997) Rare-earth elements in apatite: uptake from H_2O-bearing phosphate-fluoride melts and the role of volatile components. Geochim Cosmochim Acta 61:4745–4760
Fleet ME, Liu XY, Pan YM (2000) Site preference of rare earth elements in hydroxyapatite $[Ca_{10}(PO_4)_6(OH)_2]$. J Solid State Chem 149:391–398
Fleet ME, Liu XY, Shieh SR (2010) Structural change in lead fluorapatite at high pressure. Phys Chem Miner 37:1–9
Gatta GD, Lee Y, Kao CC (2009) Elastic behavior of vanadinite, $Pb_{10}(VO_4)_6C_{l2}$, a microporous non-zeolitic mineral. Phys Chem Miner 36:311–317
Gilmore RS, Katz JL (1982) Elastic properties of apatites. J Mater Sci 17:1131–1141
Hadrich A, Lautie A, Mhiri T (2001) Monoclinic to hexagonal phase transition and hydroxyl motion in calcium-lead hydroxyapatites studied by Raman spectroscopy. J Raman Spectrosc 32:33–40
Hammersley J (1998) Fit2D report. European Synchrotron Radiation Facility, Grenoble
He Q, Liu X, Hu XM, Deng LW, Chen ZQ, Li BS, Fei YW (2012) Solid solutions between lead fluorapatite and lead fluorvandate apatite: compressibility determined by using a diamond-anvil cell coupled with synchrotron X-ray diffraction. Phys Chem Miner 39:219–226
Hughes JM, Cameron M, Mariano AN (1991) Rare-earth-element ordering and structural variations in natural rare-earth-bearing apatites. Am Miner 76:1165–1173
Irving AJ (1978) A review of experimental studies of crystal/liquid trace element partitioning. Geochim Cosmochim Acta 42:743–770
Larson AC, Von Dreele RB (2004) General structure analysis system (GSAS). Los Alamos National Laboratory Report LAUR 86-748
Lee KKM, O'Neill B, Panero WR, Shim SH, Benedetti LR, Jeanloz R (2004) Equations of state of the high-pressure phases of a natural peridotite and implications for the earth's lower mantle. Earth Planet Sci Lett 223:381–393
Liu X, Shieh SR, Fleet ME, Akhmetov A (2008) High-pressure study on lead fluorapatite. Am Miner 93:1581–1584
Liu X, Shieh SR, Fleet ME, Zhang LF, He Q (2011a) Equation of state of carbonated hydroxyapatite at ambient temperature up to 10 GPa: significance of carbonate. Am Miner 96:74–80
Liu X, Fleet ME, Shieh SR, He Q (2011b) Synthetic lead bromapatite: X-ray structure at ambient pressure and compressibility up to about 20 GPa. Phys Chem Miner 38:397–406
Mao HK, Bell PM, Shaner JW, Steinberg DJ (1978) Specific volume measurements of Cu, Mo, Pt, and Au and calibration of ruby R1 fluorescence pressure gauge for 0.006 to 1 Mbar. J Appl Phys 49:3276–3283
Matsukage KN, Ono S, Kawamoto T, Kikegawa T (2004) The compressibility of a natural apatite. Phys Chem Miner 31:580–584
Murayama JK, Makai S, Kato M, Kumazawa M (1986) A dense polymorph of $Ca_3(PO_4)_2$: a high-pressure phase of apatite decomposition and its geochemical significance. Phys Earth Planet Interiors 44:293–303
Nakayama S, Sakamoto M (1998) Electrical properties of new type high oxide ionic conductor $RE_{10}Si_6O_{27}$ (RE = La, Pr, Nd, Sm, Gd, Dy). J Eur Ceram Soc 18:1413–1418
Nakayama S, Kageyama T, Aono H, Sadaoka Y (1995) Ionic conductivity of lanthanoid silicates, $Ln_{10}(SiO_4)_6O_3$ (Ln = La, Nd, Sm, Gd, Dy, Y, Ho, Er and Yb). J Mater Chem 5:1801–1805
Nakayama S, Sakamoto M, Higuchi M, Kodaira K, Sato M, Kakita S, Suzuki T, Itoh K (1999) Oxide ionic conductivity of apatite type $Nd_{9.33}(SiO_4)_6O_2$ single crystal. J Eur Ceram Soc 19:507–510
Pan Y, Fleet ME (2002) Compositions of the apatite-group minerals: substitution mechanisms and controlling factors. Rev Miner Geochem 48:13–49
Prowatke S, Klemme S (2006) Trace element partitioning between apatite and silicate melts. Geochim Cosmochim Acta 70:4513–4527
Serret A, Cabanas MV, Vallet-Regi M (2000) Stabilization of calcium oxyapatites with lanthanum (III)-created anionic vacancies. Chem Mater 12:3836–3841
Thomson P, Cox DE, Hastings JB (1987) Rietveld refinement of Debye-Scherrer synchrotron X-ray data from Al_2O_3. J Appl Crystallogr 20:79–83
Toby BH (2001) EXPGUI, a graphical user interface for GSAS. J Appl Crystallogr 34:210–213
Wang C, Liu XY, Fleet ME, Feng SH, Xu RR (2006) High-pressure synthesis and single-crystal structure refinement of gadolinium holmium silicate hydroxyapatite $Gd_{4.33}Ho_{4.33}(SiO_4)_6(OH)_2$. J Solid State Chem 179:2245–2250
Watson EB, Capobainco CJ (1981) Phosphorus and the rare-earth elements in felsic magmas: an assessment of the role of apatite. Geochim Cosmochim Acta 45:2349–2358
Watson EB, Green DH (1981) Apatite/liquid partition coefficients for the rare-earth elements and strontium. Earth Planet Sci Lett 56:405–421
Watson EB, Harrison TM (1984) Accessory minerals and the geochemical evolution of crustal magmatic systems: a summary and prospectus of experimental approaches. Phys Earth Planet Interiors 35:19–30
Wei SY, Ma MN, Fan DW, Yang J, Zhou WG, Li BS, Chen ZQ, Xie HS (2013) Compressibility of mimetite and pyromorphite at high pressure. High Press Res 33:27–34
Wendt AS, Vidal O, Chadderton LT (2002) Experimental evidence for the pressure dependence of fission track annealing in apatite. Earth Planet Sci Lett 201:593–607
White TJ, Dong ZL (2003) Structural derivation and crystal chemistry of apatites. Acta Crystallogr B 59:1–16
Xie H, Zhang Y, Xu HG, Hou W, Guo J, Zhao H (1993) A new method of measurement for elastic wave velocities in minerals and rocks at high temperature and high pressure and its significance. Sci China, Ser B 36:1276–1280
Zhai SM, Xue WH, Yamazaki D, Shan SM, Ito E, Tomioka N, Shimojuku A, Funakoshi K (2011) Compressibility of strontium orthophosphate $Sr_3(PO_4)_2$ at high pressure. Phys Chem Miner 38:357–361